Available online at www.sciencedirect.com
SCIENCE DIRECT®
Physica D 201 (2005) 1–26
PHYSICA D
www.elsevier.com/locate/physd

High-order shock-capturing methods for modeling dynamics of the solar atmosphere

Steve Bryson[a], Alexander Kosovichev[b], Doron Levy[c,*]

[a] *Program in Scientific Computing/Computational Mathematics, Stanford University and the NASA Advanced Supercomputing Division, NASA Ames Research Center, Moffett Field, CA 94035-1000, USA*
[b] *W.W. Hansen Experimental Physics Laboratory, Stanford University, Stanford, CA 94305-2125, USA*
[c] *Department of Mathematics, Stanford University, Stanford, CA 94305-2125, USA*

Received 2 July 2004; received in revised form 22 December 2004; accepted 22 December 2004
Communicated by C.K.R.T. Jones

Abstract

We use one-dimensional high-order central shock-capturing numerical methods to study the response of various model solar atmospheres to forcing at the solar surface. The dynamics of the atmosphere is modeled with the Euler equations in a variable-sized flux tube in the presence of gravity. We study dynamics of the atmosphere suggestive of spicule formation and coronal oscillations. These studies are performed on observationally derived model atmospheres above the quiet sun and above sunspots.

To perform these simulations, we provide a new extension of existing second- and third-order shock-capturing methods to irregular grids. We also solve the problem of numerically maintaining initial hydrostatic balance via the introduction of new variables in the model equations and a careful initialization mechanism.

We find several striking results: all model atmospheres respond to a single impulsive perturbation with several strong shock waves consistent with the rebound-shock model. These shock waves lift material and the transition region well into the initial corona, and the sensitivity of this lift to the initial impulse depends nonlinearly on the details of the atmosphere model. We also reproduce an observed 3 min coronal oscillation above sunspots as well as 5 min oscillations above the quiet sun.

MSC: Primary 85A30; Secondary 65M06

Keywords: Coronal oscillations; Spicules; Rebound-shock models; High-order central-upwind schemes; Balance laws; Conservation laws; Source terms

* Corresponding author. Tel.: +1 650 723 4157; fax: +1 650 725 4066.
E-mail addresses: bryson@nas.nasa.gov (S. Bryson), sasha@quake.stanford.edu (A. Kosovichev), dlevy@math.stanford.edu (D. Levy).

0393-0440/$ – see front matter © 2004 Elsevier B.V. All rights reserved.
doi:10.1016/j.physd.2004.12.006

1. Introduction

This paper investigates the response of the solar atmosphere to impulsive forcing at the solar surface using initial conditions derived from observationally based atmosphere models. Impulsive forcing is studied because it provides insight into the natural modes of oscillation of the solar atmosphere, and because there are occasional observed impulsive phenomena, such as small solar flares, spicules, etc. Impulsive forcing is believed to be mostly caused by magnetic stresses, such as those resulting from magnetic reconnection, local dynamo action, the emergence of magnetic flux tubes from the solar interior and interaction between flux tubes and granular convection. We look at a range of parameters that define the forcing function for each atmosphere model. We simulate the response of previously published observationally based model atmospheres above the quiet sun and above sunspots. Various phenomena that appear in our simulations correspond to observed phenomena on the sun. Specifically, our simulations show behavior corresponding to *spicules*, narrow, jet-like features observed in the solar atmosphere, and oscillations in the upper atmosphere. We find that the details of these phenomena depend on the atmosphere model.

The dominant feature in our simulations is strong shock waves that propagate upward, lifting material from the lower atmosphere and causing oscillations of atmospheric materials. Because of these strong shocks, we perform our simulations using high-resolution central shock-capturing schemes. These schemes provide reliable approximations to solutions of the model equations in the presence of strong shocks while avoiding spurious numerical oscillations. We extend existing methods to computational meshes which have variable grid spacing. We also use new variables defined to facilitate numerical maintenance of hydrostatic equilibrium.

One important result of our simulations is the observation that the height of the lifted material depends nonlinearly on the details of the initial atmospheric model. A second result is that when we use the quiet sun atmosphere model, we observe a period of particle oscillations is in the 6 min range while if we initialize our simulations using a sunspot model we see oscillations in the 4 min range. This is strikingly similar to observations of coronal oscillations in the solar atmosphere [2].

Our simulations are based on the quasi-one-dimensional Euler equations applied to an initially hydrostatic atmosphere in a magnetic flux tube whose area increases with height. This model ignores heating, except for the input background heating needed to maintain the initial atmosphere contained in the initial conditions. This model also ignores radiative energy loss, ionization terms, and thermal diffusion. We neglect magnetic fields beyond their role in defining the geometry of the flux tube. Our lack of inclusion of energy loss precludes the study of continuous forcing, because without energy loss terms such forcing would increase the energy of the atmosphere, causing it to expand without bound. We therefore restrict our study to impulsive forcing. We will add energy loss terms and study continuous forcing in a future work.

The structure of this paper is as follows: In Section 1.1 we discuss basic properties of the solar atmosphere, describing its structure and summarizing the observed phenomena of interest to this paper. Section 2 presents the physical model that underlies our simulation. Section 3 introduces our numerical method, including a discussion of initial and boundary conditions, and the computational mesh. New second- and third-order reconstructions on irregular meshes are presented in Section 3.2. In Section 3.4 we present a new technique for maintaining initial hydrostatic equilibrium. Section 4 presents our results, focusing on the match between our simulations and observed properties of the solar atmosphere. We speculate on physical interpretations of our results in Section 4.2.1.

1.1. The solar atmosphere

The solar atmosphere is a dynamic environment with high-energy phenomena occurring on many scales. At the base of the solar atmosphere is the *photosphere*, the surface of sun's convective outer layer. The photosphere is roughly divided into two types of regions, *quiet* and *active*. The dominant features of the quiet photosphere are its temperature, about 6000 K, and *granulations*, which are currently understood as the surface of convective cells

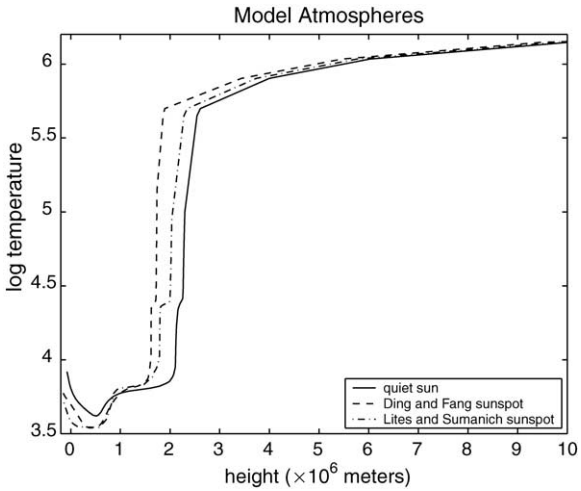

Fig. 1. Temperature profiles in the model atmospheres we use in our simulations.

rising from below. The surface of the photosphere has been observed to rise and fall with velocities in the range of 1 km/s, and with a period of about 5 min. Active regions are associated with sunspots, which are regions of lower temperature, and very strong magnetic fields.

Above the photosphere, magnetic fields form *magnetic flux tubes*, where a fixed number of magnetic field lines are confined by hydrodynamic pressure into a tube. Since hydrodynamic pressure drops with increasing height, the flux tube will in general expand with altitude, requiring a quasi-one-dimensional simulation. Though many flux tubes are curved and closed, following magnetic loops, we will consider the simpler case of open magnetic flux tubes pointing radially upward.

Above the photosphere, the solar atmosphere has a strongly stratified structure. The most striking feature of this stratification is the variation of temperature with height. For example above quiet regions, after slowly dropping in temperature to about 4700 K at about 3×10^5 m, at 2×10^6 m there is a strong rise to about 10^6 K within a few kilometers. The layer within which this dramatic rise in temperature occurs is called the *transition region*. The solar atmosphere below the transition region and above the photosphere is called the *chromosphere*, and above is the *corona*.

One-dimensional models of the solar atmosphere have been developed, based on observed temperatures, densities and the requirement of hydrostatic equilibrium. The assumption of hydrostatic equilibrium is only approximately justified, since significant down- and up-flows have been observed. Models have been developed for the atmosphere above quiet regions [17] and sunspots [4,9]. Fig. 1 shows the temperature profiles for the models that we use in our simulations.

In the simulations described in this paper we begin with an atmosphere in hydrostatic equilibrium. This initial atmosphere is based on one of the model temperature profiles described above. This atmosphere is then forced by an impulse perturbation at the base of the atmosphere. There are two observed phenomena in the solar atmosphere that correspond to features that appear in our simulations.

- *Spicules*. Spicules [3,13] are narrow near-linear features that are observed on the solar limb (see Fig. 2). They seem to be cooler chromospheric material shooting up into the corona, and so can be modeled as an uplifting of the transition region in a magnetic flux tube. We will see such uplifting in our simulations.
- *Coronal oscillations*. Particle oscillations in the corona have been observed to have periods of about 5 min above quiet regions and 3 min above sunspots [2].

Fig. 2. Spicules near the solar limb, seen as darker linear features against the solar surface. The spicules appear darker in this narrow-band hydrogen-alpha image because their light is blue shifted due to their motion towards the observer. Photo credit: National Solar Observatory/Sacramento Peak.

We describe these observations in more detail in Section 4 where we compare them directly with our simulations.

1.2. Previous simulations

There is a sizable literature of simulations similar to those presented in this paper, most of which attempt to model spicule formation. Early attempts to model spicules as a ballistic uprise of the chromosphere into the corona due to a very large (60 km/s) initial impulse are found in [11,15]. These simulations used vertical straight flux tubes. Smaller impulses leading to a rise via the rebound shock phenomenon are considered in [1,5,6], some of which include expanding flux tubes. These simulations are extended in [14] by adding radiative energy loss, heating and heat conduction terms. These simulations used either the quiet sun VAL model or a simplified model of the solar atmosphere.

Our paper extends the above work in two ways: we perform these simulations on recently published atmosphere models above sunspots, comparing the results with those above the quiet sun. We also study coronal particle oscillations in response to our impulsive forcing in the various atmosphere models. Our primary objects of study are the relative behavior of both spicule formation and coronal particle oscillation in the various atmosphere models.

2. The model

The quasi-one-dimensional hydrodynamic equations for material in a flux tube of area $A(x, t)$ in gravity are written in terms of density $\rho(x, t)$, velocity $u(x, t)$ and kinetic plus thermal energy $E(x, t)$ as

$$\begin{pmatrix} A\rho \\ A\rho u \\ AE \end{pmatrix}_t + \begin{pmatrix} A\rho u \\ A\rho u^2 \\ A(E+p)u \end{pmatrix}_x = \begin{pmatrix} 0 \\ -Ap_x - g(x)A\rho + F(x,t)A\rho \\ -g(x)A\rho u + F(x,t)A\rho u \end{pmatrix}, \tag{2.1}$$

where $g(x)$ is the gravitational acceleration and the pressure $p(x, t)$ is given by the equation of state $p = (\gamma - 1)(E - (1/2)\rho u^2)$ with $\gamma = 5/3$. The temperature T is given by $p = R'\rho T$, where R' is the universal gas constant. $F(x, t)$ is a forcing term which perturbs the base of the solar atmosphere in our numerical experiments. We describe our specific forcing function in Section 4.

In order to use numerical methods that were developed for conservation laws, we rewrite (2.1) as a balance law (conservation law with source)

$$\begin{pmatrix} \rho \\ \rho u \\ E \end{pmatrix}_t + \begin{pmatrix} \rho u \\ \rho u^2 + p \\ (E+p)u \end{pmatrix}_x = \begin{pmatrix} -\rho u A^{-1} A_x - \rho A^{-1} A_t \\ -\rho u^2 A^{-1} A_x - \rho u A^{-1} A_t - g(x)\rho + F(x,t)\rho \\ -(E+p)u A^{-1} A_x - E A^{-1} A_t - g(x)\rho u + F(x,t)\rho u \end{pmatrix}. \tag{2.2}$$

This form makes explicit that the scale of the flux tube area does not affect the dynamics. Following previous authors [5,14] we consider static flux tubes so $A_t = 0$.

For our flux tube geometry, based on the model given in [14], we use the functional approximation

$$A(x) = A_0[1 + b(a(x) - a_0)]^2. \tag{2.3}$$

Here $b = 3.2$, $a(x) = \tanh(s(x - x_0))$ with $s = 10^{-6}$ and $x_0 = 1.5 \times 10^6$, and $a_0 = a(0)$. $A_0 = A(0)$ is the area of the flux tube at the base of the atmosphere, but does not appear in the simulation. Therefore

$$\frac{A'(x)}{A(x)} = \frac{2bs(1 - a(x)^2)}{1 + b(a(x) - a_0)}.$$

3. The numerical method

In this paper we use high-order, non-oscillatory central schemes designed to solve systems of conservation laws with source terms of the form

$$q_t + f(q)_x = S(q, x). \tag{3.1}$$

Here $q \in \mathbb{R}^p$ is a p-dimensional solution vector, f is the flux function, and $S \in \mathbb{R}^p$ is the p-dimensional vector of source terms. The solution of (3.1) may become singular in finite time, which in turn requires careful study when dealing with numerical approximations.

Our approach for solving (3.1) is based on extending the semi-discrete central-upwind scheme of Kuragnov et al. (KNP) [8] to irregular grids. The KNP method is a simple efficient scheme with less dissipation than fully central schemes, and has desirable stability properties. Any such scheme is composed of a numerical flux, a piecewise-polynomial reconstruction and an ODE solver. The order of accuracy of the reconstruction and the ODE solver determine the order of accuracy of the method. Below we address all three ingredients, with a particular focus on our new high-order reconstructions on irregular grids.

Throughout this section we assume a one-dimensional grid with irregularly spaced nodes x_j. The distance between consecutive grids points is denoted as $\Delta x_j := x_{j+1} - x_j$. We define $x_{j+1/2} := (x_j + x_{j+1})/2$ and the cell $I_j = [x_{j-1/2}, x_{j+1/2}]$. For any function $f(x)$ we use the notation $f_j := f(x_j)$. The cell average of q in the cell I_j is given by

$$\bar{q}_j := \frac{1}{x_{j+1/2} - x_{j-1/2}} \int_{x_{j-1/2}}^{x_{j+1/2}} q(x)\,\mathrm{d}x.$$

We assume that the cell-averages $\bar{q}_j^n$ are known at time t^n. The first step in the derivation of the approximate solution is to generate a piecewise-polynomial reconstruction from these cell-averages. Such a global reconstruction is defined as

$$\tilde{q}(x) = \sum_j \tilde{q}_j(x)\chi_{I_j}(x), \tag{3.2}$$

where $\chi_{I_j}(x)$ is the characteristic function of I_j, and $\tilde{q}_j(x)$ are polynomials of a suitable degree. The construction of admissible $\tilde{q}_j$ will be discussed in Section 3.2. For the time being, it is sufficient to assume that a reconstruction of the form (3.2) is known.

We denote the point-values of $\tilde{q}$ at the interfaces of the cell I_j by

$$q^+_{j+1/2} := \tilde{q}_{j+1}(x_{j+1/2}), \qquad q^-_{j+1/2} := \tilde{q}_j(x_{j+1/2}).$$

3.1. The KNP central-upwind method

It is straightforward to extend the semi-discrete central scheme of [8] to irregular grids. When written in a conservative form this scheme takes the form

$$\frac{\mathrm{d}\bar{q}_j}{\mathrm{d}t} = -\frac{H_{j+1/2} - H_{j-1/2}}{x_{j+1/2} - x_{j-1/2}} + \bar{S}_j, \tag{3.3}$$

where $\bar{S}_j$ is a discretization of the averaged value of the source term in I_j and the numerical flux $H_{j+1/2}$ is given by

$$H_{j+1/2} = \frac{a^+_{j+1/2} f(q^-_{j+1/2}) + a^-_{j+1/2} f(q^+_{j+1/2})}{a^+_{j+1/2} + a^-_{j+1/2}} - \frac{a^+_{j+1/2} a^-_{j+1/2}}{a^+_{j+1/2} + a^-_{j+1/2}} [q^+_{j+1/2} - q^-_{j+1/2}].$$

The local speeds of propagation of information from the discontinuities on the interfaces of the cells, $a_{j\pm1/2}$, are given by

$$a^+_{j+1/2} = \max\left(\lambda_k\left(\frac{\partial f}{\partial q}\right), 0\right), \qquad a^-_{j+1/2} = \left|\min\left(\lambda_k\left(\frac{\partial f}{\partial q}\right), 0\right)\right|.$$

Here $\lambda_k(\partial f/\partial q)$ denote the eigenvalues of the Jacobian of f evaluated at $x_{j+1/2}$. In the case of problem (2.2), we have

$$a^+_{j+1/2} = \max(u - c, u, u + c, 0), \qquad a^-_{j+1/2} = |\min(u - c, u, u + c, 0)|,$$

where $c = \sqrt{\gamma p/\rho}$ is the speed of sound and all fields are evaluated at $x_{j+1/2}$.

We approximate the cell-average of the source term $\bar{S}_j$ as $S(\bar{\rho}_j, \bar{u}_j, \bar{E}_j, x_j)$. This amounts to a first-order quadrature approximation to the cell average. The $O(\Delta x_j)$ error from this approximation appears in the terms containing the flux tube area variation and the gravitational acceleration $g(x)$. This error is acceptable since the flux tube model (2.3) is itself only qualitative. While we compute the gravitational acceleration $g(x)$ for each cell, it is slowly varying and so is approximately constant in each cell.

3.2. Reconstructions and order of accuracy

In this section we introduce the new second- and third-order reconstructions for irregular grids that we use in the scheme (3.3). In spite of the uncertainties that exist in the model atmospheres we use for our initial conditions as well as the overall simplified nature of our model, high-order methods are valuable since they enable us to conduct long-time simulations with well-resolved shock structures.

Our second-order reconstruction, when used in (3.3), is highly efficient and leads to a method that is total variation diminishing (TVD). The TVD property assures that spurious numerical oscillations will not increase from one timestep to another. The third-order method, when used in (3.3) provides higher resolution and leads to a number of extrema diminishing (NED) method on regular grids. While the NED property does not guarantee that existing oscillations will not grow, it does assure us that new numerical oscillations will not be introduced. Though we have

not demonstrated that the NED property holds for irregular grids, the computational mesh we use in our simulations is regular in the region of greatest interest.

The reconstruction $\tilde{q}_j(x)$ in the cell I_j should satisfy the following requirements:

- *Conservation*

$$\frac{1}{x_{j+1/2} - x_{j-1/2}} \int_{x_{j-1/2}}^{x_{j+1/2}} \tilde{q}_j(x)\,\mathrm{d}x = \bar{q}_j.$$

  While any linear reconstruction satisfies this property on a regular grid, this will not be automatically true when the grid has variable spacing.
- *Accuracy*. $\tilde{q}_j$ is an rth-order accurate reconstruction. On a regular grid with grid spacing Δx this amounts to

$$\tilde{q}_j(x) = q(x) + \mathrm{O}(\Delta x^r), \quad x \in I_j.$$

- *Oscillation minimizing*. Spurious numerical oscillations should be avoided.

3.2.1. A second-order reconstruction

Second-order reconstructions are provided by piecewise-linear interpolants, with a different interpolant for each cell I_j. A linear interpolant that is conservative in I_j for any D_j is given by

$$\tilde{q}_j(x) = \bar{q}_j + D_j \left(x - \left(x_j + \frac{1}{4} \left(\Delta x_j - \Delta x_{j-1} \right) \right) \right). \tag{3.4}$$

The discrete derivative, D_j, is taken as

$$D_j = \mathrm{MinMod}\left(4\frac{\bar{q}_j - \bar{q}_{j-1}}{\Delta x_j + 2\Delta x_{j-1} + \Delta x_{j-2}}, 4\frac{\bar{q}_{j+1} - \bar{q}}{\Delta x_{j+1} + 2\Delta x_j + \Delta x_{j-1}} \right), \tag{3.5}$$

where the MinMod limiter is defined as

$$\mathrm{MinMod}(q_1, \ldots, q_n) = \begin{cases} \min(q_1, \ldots, q_n), & q_i > 0, \forall i, \\ \max(q_1, \ldots, q_n), & q_i < 0, \forall i, \\ 0, & \text{otherwise.} \end{cases}$$

See [16] for a discussion of nonlinear limiters on uniform grids. The expression (3.4) now provides the required values at the cell interfaces:

$$q^-_{j+1/2} = \tilde{q}_j(x_{j+1/2}) = \bar{q}_j + \frac{1}{4} D_j(\Delta x_j + \Delta x_{j-1}),$$

$$q^+_{j+1/2} = \tilde{q}_{j+1}(x_{j+1/2}) = \bar{q}_{j+1} - \frac{1}{4} D_{j+1}(\Delta x_j + \Delta x_{j+1}).$$

Lemma 3.1. *The reconstruction (3.4) and (3.5) is total variation preserving.*

Proof. Our reconstruction is $R(v) = \sum_j \tilde{q}_j(x)\chi_j(x)$, where $\tilde{q}_j$ is given by (3.4). Then

$$\mathrm{TV}(R(v)) = \sum_j \left[|D_j| \left(\frac{\Delta x_j + \Delta x_{j-1}}{2} \right) + \left| \bar{q}_j - \bar{q}_{j+1} + \frac{D_j}{4}(\Delta x_{j+1} + \Delta x_j) + \frac{D_{j+1}}{4}(\Delta x_j + \Delta x_{j+1}) \right| \right].$$

It is easy to verify that D_j defined in (3.5) satisfies

1. $\mathrm{sgn}(D_j) = \mathrm{sgn}(D_{j+1}) = \mathrm{sgn}(\bar{q}_{j+1} - \bar{q}_j)$.
2. $\frac{1}{4}|(\Delta x_{j-1} + \Delta x_j)D_j + (\Delta x_j + \Delta x_{j+1})D_{j+1}| \le |\bar{q}_{j+1} - \bar{q}_j|$.

Then (assuming periodic boundary conditions)

$$\begin{aligned}\mathrm{TV}(R(v)) &= \sum_j \left[|D_j| \left(\frac{\Delta x_j + \Delta x_{j-1}}{2} \right) + |\bar{q}_j - \bar{q}_{j+1}| - \frac{|D_j|}{4}(\Delta x_{j+1} + \Delta x_j) - \frac{|D_{j+1}|}{4}(\Delta x_j + \Delta x_{j+1}) \right] \\ &= \sum_j |\bar{q}_j - \bar{q}_{j+1}| + \sum_j |D_j| \frac{\Delta x_{j-1} + \Delta x_j}{4} - \sum_j |D_{j+1}| \frac{\Delta x_j + \Delta x_{j+1}}{4} = \mathrm{TV}(v). \qquad \square\end{aligned}$$

3.2.2. A third-order reconstruction

The third-order method from [7], based on [10], uses a linear combination of a linear interpolant $L_j(x)$ and a quadratic interpolant $Q_j(x)$ that is third-order accurate in smooth regions. Whenever a discontinuity is present, the order of the reconstruction is reduced by choosing one linear interpolant from the appropriate side of the discontinuity. This latter choice minimizes spurious numerical oscillations. The reconstruction of [7] is given in terms of the convex combination

$$\tilde{q}_j(x) := (1 - \theta_j)L_j(x) + \theta_j Q_j(x), \tag{3.6}$$

where

$$\theta_j := \begin{cases} \min\left\{ \dfrac{M_{j+1/2} - L_j(x_{j+1/2})}{M_j - L_j(x_{j+1/2})}, \dfrac{m_{j-1/2} - L_j(x_{j-1/2})}{m_j - L_j(x_{j-1/2})}, 1 \right\}, & \bar{q}_{j-1} < \bar{q}_j < \bar{q}_{j+1}, \\ \min\left\{ \dfrac{M_{j-1/2} - L_j(x_{j-1/2})}{M_j - L_j(x_{j-1/2})}, \dfrac{m_{j+1/2} - L_j(x_{j+1/2})}{m_j - L_j(x_{j+1/2})}, 1 \right\}, & \bar{q}_{j-1} > \bar{q}_j > \bar{q}_{j+1}, \\ 1, & \text{otherwise}, \end{cases}$$

and

$$\begin{aligned} &M_j = \max\{Q_j(x_{j+1/2}), Q_j(x_{j-1/2})\}, \qquad m_j = \min\{Q_j(x_{j+1/2}), Q_j(x_{j-1/2})\}, \\ &M_{j\pm1/2} = \max\{\tfrac{1}{2}(L_j(x_{j\pm1/2}) + L_{j\pm1}(x_{j\pm1/2})), Q_{j\pm1}(x_{j\pm1/2})\}, \\ &m_{j\pm1/2} = \min\{\tfrac{1}{2}(L_j(x_{j\pm1/2}) + L_{j\pm1}(x_{j\pm1/2})), Q_{j\pm1}(x_{j\pm1/2})\}. \end{aligned}$$

We now extend the method (3.6) to non-uniform grids. The linear function, $L_j(x)$, is taken as the conservative reconstruction (3.4) with (3.5). The quadratic function, $Q_j(x)$, is replaced by

$$Q_j(x) = A_j + B_j(x - (x_j + x_0)) + C_j(x - (x_j + x_0))^2, \tag{3.7}$$

where

$$\begin{aligned} &x_0 = \frac{1}{4}(\Delta x_j - \Delta x_{j-1}), \qquad A_j = \bar{q}_j - \frac{1}{48}\gamma_j^2 C_j, \\ &B_j = 2\alpha_j[-\beta_j(\Delta x_{j-1} + 3\Delta x_j + 2\Delta x_{j+1})\bar{q}_{j-1} + \beta_j\beta_{j+1}\mu_j\bar{q}_j + \beta_{j+1}(2\Delta x_{j-2} + 3\Delta x_{j-1} + \Delta x_j)\bar{q}_{j+1}], \\ &C_j = 12\alpha_j[\beta_j\bar{q}_{j-1} + \beta_j\beta_{j+1}\eta_j\bar{q}_j + \beta_{j+1}\bar{q}_{j+1}]. \end{aligned}$$

Here $\gamma_j = \Delta x_j + \Delta x_{j-1}$,

$$\alpha_j = \frac{1}{(\Delta x_{j-2} + 2\Delta x_{j-1} + 2\Delta x_j + \Delta x_{j+1})}, \qquad \beta_j = \frac{1}{\Delta x_{j-2} + 2\Delta x_{j-1} + \Delta x_j},$$
$$\eta_j = -(\Delta x_{j-2} + 3\Delta x_{j-1} + 3\Delta x_j + \Delta x_{j+1}),$$

and

$$\mu_j = (2\Delta x_{j-2} + 5\Delta x_{j-1} + 5\Delta x_j + 2\Delta_{j+1})(-\Delta x_{j-2} - \Delta x_{j-1} + \Delta x_j + \Delta x_{j+1}).$$

It is easy to verity that the interpolant (3.7) is conservative and third-order accurate on I_j. Using (3.7) we get that the point values at the cell interfaces are

$$Q_j(x_{j+1/2}) = -\alpha_j\beta_j\gamma_j\gamma_{j+1}\bar{q}_{j-1} + \left(1 + \frac{1}{2}\alpha_j\beta_j\beta_{j-1}\gamma_j(\gamma_j\eta_j + \mu_j)\right)\bar{q} + \alpha_j\frac{\beta_{j+1}}{\beta_j}\gamma_j\bar{q}_{j+1},$$

and

$$Q_j(x_{j-1/2}) = \alpha_j\frac{\beta_j}{\beta_{j+1}}\gamma_j\bar{q}_{j-1} + \left(1 + \frac{1}{2}\alpha_j\beta_j\beta_{j-1}\gamma_j(\gamma_j\eta_j - \mu_j)\right)\bar{q}_j - \alpha_j\beta_{j+1}\gamma_j\gamma_{j-1}\bar{q}_{j+1}.$$

3.3. Time integration

The time stepping is performed by either a second- or third-order TVD Runge–Kutta method from [12]. Given data q_j^n at time t^n, we advance to the next time step by solving an ODE of the form

$$\frac{\mathrm{d}q_j}{\mathrm{d}t} = F(q_j). \tag{3.8}$$

A second-order TVD RK method for (3.8) is

$$q^{(1)} = q^n + \Delta t F(q^n), \qquad q^{n+1} = \frac{1}{2}(q^n + q^{(1)} + \Delta t F(q^{(1)})).$$

A third-order TVD RK method for (3.8) is

$$q^{(1)} = q^n + \Delta t F(q^n), \qquad q^{(2)} = \frac{3}{4}q^n + \frac{1}{4}(q^{(1)} + \Delta t F(q^{(1)})), \qquad q^{n+1} = \frac{1}{3}q^n + \frac{2}{3}(q^{(2)} + \Delta t F(q^{(2)})).$$

Each time step is set to

$$\Delta t = \beta \max_j \frac{\Delta x_j}{\sigma(J_j)},$$

where $\sigma(J_j)$ is the spectral radius of the Jacobian $J = \partial f/\partial q$ evaluated at x_j. The parameter β is taken in our simulations as $\beta = 0.45$.

3.4. Hydrostatic equilibrium

We assume hydrostatic equilibrium at initialization and at the computational domain boundaries. This implies that $u = 0$ and there is no time evolution so long as hydrostatic equilibrium is maintained. Therefore hydrostatic equilibrium relates pressure and density via (2.2) as

$$\frac{\mathrm{d}p(x)}{\mathrm{d}x} = -g(x)\rho(x) = -\frac{g(x)p(x)}{R'T(x)}. \tag{3.9}$$

We use the temperature profile $T(x)$ and pressure at the bottom of the atmosphere $p(0) = R'\rho(0)T(0)$ that are given by an atmosphere model to solve (3.9) for the hydrostatic pressure profile $p(x)$.

3.4.1. Hydrostatic balance

In order to obtain numerical hydrostatic balance, we modify the model (2.2) through a change of variables. We assume that we are given an initial density $\rho_0(x)$ and energy $E_0(x)$ in hydrostatic equilibrium as described in Section 3.4.2. We define the variables $\hat{\rho} := \rho - \rho_0$ and $\hat{E} := E - E_0$ and write the system (2.2) in the mathematically equivalent form

$$\begin{pmatrix} \hat{\rho} \\ \rho u \\ \hat{E} \end{pmatrix}_t + \begin{pmatrix} (\hat{\rho}+\rho_0)u \\ (\hat{\rho}+\rho_0)u^2 + p \\ (\hat{E}+E_0+p)u \end{pmatrix}_x = \begin{pmatrix} -(\hat{\rho}+\rho_0)uA^{-1}A_x \\ -(\hat{\rho}+\rho_0)(u^2A^{-1}A_x + g - F) \\ -(\hat{E}+E_0+p)uA^{-1}A_x - (g-F)(\hat{\rho}+\rho_0)u \end{pmatrix}, \tag{3.10}$$

with $p := (\gamma-1)(\hat{E} + E_0 - (1/2)(\hat{\rho}+\rho_0)u^2)$. Here we define $u := \rho u/(\hat{\rho}+\rho_0)$ and use the fact that hydrostatic equilibrium implies that the flux tube is static so $A_t = 0$. With these new variables, $\hat{\rho} = \hat{E} = 0$ as long as the system remains in hydrostatic equilibrium, i.e. satisfies (3.9) with $u = 0$. We estimate $\rho_0(x_{j\pm1/2})$ and $E_0(x_{j\pm1/2})$ at the cell interfaces using the interpolants described in Section 3.2. As described in Section 3.4.2, if $\rho_0(x)$ is defined by (3.12), then our numerical method (2.2) will remain in hydrostatic balance as long as $u = 0$.

3.4.2. Hydrostatic initialization

We use (3.9) to initialize our simulations in hydrostatic equilibrium given a temperature profile specified by a solar model. Eq. (3.9) is integrated on a high-resolution grid using a standard fourth-order Runge–Kutta method, then linearly interpolated onto the actual computational grid of the simulation. This process gives an initial pressure profile $p_0(x)$ which is transformed into an energy profile via $E_0(x) = p_0(x)/(\gamma-1)$.

The initial density profile $\rho_0(x)$ is determined by the requirement of numerical hydrostatic equilibrium $u = 0$ in our method (3.3). In this case we have $a^+_{j+1/2} = a^-_{j+1/2} = c_{j+1/2}$. Inserting these conditions into (3.3) applied to our model (2.2) (suppressing the subscript 0 on p_0 for clarity), we obtain

$$\frac{1}{2(x_{j+1/2}-x_{j-1/2})}\left\{ \begin{pmatrix} \rho^- - \rho^+ \\ p^- + p^+ \\ E^- - E^+ \end{pmatrix}_{j+1/2} - \begin{pmatrix} \rho^- - \rho^+ \\ p^- + p^+ \\ E^- - E^+ \end{pmatrix}_{j-1/2} \right\} = \begin{pmatrix} 0 \\ -g\rho \\ 0 \end{pmatrix}_j. \tag{3.11}$$

We therefore have hydrostatic balance in the second component if we initialize the density term in the source as

$$(\rho_0)_j = -\frac{1}{2g_j(x_{j+1/2}-x_{j-1/2})}[p^-_{j+1/2} + p^+_{j+1/2} - (p^-_{j-1/2} + p^+_{j-1/2})]. \tag{3.12}$$

The first and third components of (3.11) will vanish if we use the variables defined in Section 3.4.1 so long as hydrostatic equilibrium is satisfied at x_j. Therefore if we initialize ρ according to (3.12), $\hat{\rho} = \rho u = \hat{E} = 0$ and $E_0 = p_0/(\gamma-1)$, then the method (3.3) applied to (3.10) will maintain hydrostatic equilibrium.

Remark 3.2. Eq. (3.12) is a natural discretization of the cell average using the cell interface values $p_{j\pm1/2}$:

$$\frac{1}{x_{j+1/2}-x_{j-1/2}}\int_{j-1/2}^{j+1/2} g\rho\,\mathrm{d}x = -\frac{1}{x_{j+1/2}-x_{j-1/2}}\int_{j-1/2}^{j+1/2}\frac{\partial p}{\partial x}\,\mathrm{d}x = -\frac{1}{x_{j+1/2}-x_{j-1/2}}(p_{j+1/2}-p_{j-1/2}),$$

which follows from the condition for hydrostatic equilibrium. Eq. (3.12) cannot be used to approximate the cell average of the source term after initialization because the system does not remain in hydrostatic equilibrium after we apply our forcing term. In general we approximate the source term $\bar{S}_j$ as $S(\bar{\rho}_j, \bar{u}_j, \bar{E}_j, x_j)$, see Section 3.1.

3.5. Boundary conditions

Even though we use stretched grids, placing our boundaries at great distances as described in Section 3.6, we want to limit that distance so we can use as few grid nodes as possible in the computational domain. We therefore have two issues to consider: the failure of initial hydrostatic equilibrium at the boundaries, and the problem of reflections, particularly of strong shocks. Failure of initial hydrostatic equilibrium at the boundaries will cause a wave to propagate into the domain.

Zeroth-order boundary conditions, where $q_j = q_1$ for $j < 1$ and $q_j = q_N$ for $j > N$, where N is the number of grid nodes, prevent reflections off the boundary but violate hydrostatic equilibrium. We therefore adapt a dynamic boundary condition approach, where the boundary conditions are hydrostatic until a high velocity value propagates from the interior to that boundary: if u has not risen above a threshold U since the start of the simulation then hydrostatic boundary conditions are applied. Otherwise zeroth-order boundary conditions are applied. This approach allows small reflections, which propagate slower than strong shocks thereby maximizing the time until the reflections enter the lower atmosphere region. For a typical simulation U is taken to be 1 km/s.

Hydrostatic boundary conditions are implemented by defining the field values in the ghost cells via linear interpolation of the high-resolution initialization grid described in Section 3.4.2. This requires that the high-resolution initialization grid's domain be larger than the computational domain plus any ghost cells.

3.6. The computational domain

The computational domain is divided into three regions: the lower atmosphere, which is our domain of primary interest and represents the chromosphere and lower corona, the upper corona, and a non-physical region below the solar surface. The lower atmosphere region has constant high-density grid spacing while the upper atmosphere and sub-surface regions have exponentially stretched meshes. The stretching of each stretched region is defined so that grid spacing matches that of the (non-stretched) lower atmosphere at the shared boundary, and extends to a specified distance with a specified number of nodes. In this way we can obtain high resolution in the region of interest and keep the boundaries sufficiently far away such that reflected waves do not enter the lower atmosphere region during the course of the simulation. Typical simulation values place the upper boundary of the lower atmosphere at 10^7 m and the upper corona region at 5×10^8 m.

The lower atmosphere domain is defined so that the solar surface is located at a coordinate value of 7.5×10^6 m, which corresponds to a solar radius of $r_\odot = 6.9599 \times 10^8$ m. Thus $x = 0$ corresponds to $r_0 := 6.8849 \times 10^8$ m.

The non-physical interior region. In the non-physical interior region the physics is adjusted to delay reflections from the boundary so that they do not enter the physical region during the course of the simulation. We define the gravitational acceleration in the interior region to be exponentially damped with increasing depth:

$$g(x) = \frac{GM_\odot\phi(x)}{r^2}, \quad \phi(x) = \begin{cases} 1, & x \geq 0, \\ \exp\left\{-\left(\frac{x}{0.04x_I}\right)^2\right\}, & x < 0. \end{cases}$$

Here $M_\odot$ is the solar mass, $r = r_0 + x$, and x_I is a scale defined so that $g(x) \simeq 0$ in most of the interior region. In a typical simulation x_I is typically taken as -1×10^7 m.

In hydrostatic equilibrium we have $\mathrm{d}p/\mathrm{d}x = -g\rho = -gp/R'T$ so a smaller g will lead to a smaller growth in p. We extend the temperature T into the interior as a constant: $T(x) = T(0)$ for $x < 0$. The result is a slower speed of sound so the bottom of the interior region can be closer, requiring fewer grid nodes, while still avoiding reflections off the lower boundary from entering the lower atmosphere region.

4. Results

In this section we present various results using the model and methods in this paper. We are particularly interested in the response of the solar atmosphere to a single impulse at the solar surface. Our focus is on simulations that bring out phenomena that resemble those observed in the solar atmosphere.

We consider the forcing term $F(x, t)$ in (2.2), defined as

$$F(x, t) = \frac{V}{\Delta t} X(x)\tau(t),$$

where the amplitude V has units of m/s. When we refer to, e.g. "20 m/s impulse", we mean that $V = 20$ m/s. We consider two choices for X and τ:

- X and τ as square functions with respective half-widths 10^5 m and 30 s: for $|t| \le 30$, $\tau(t) := 1$, otherwise 0, and for $|x| \le 10^5$, $X(x) := 1$, otherwise 0.
- X and τ as Gaussian functions with respective widths 10^5 m and 30 s:

$$X(x) = \exp\left\{-\left(\frac{x}{10^5}\right)^2\right\}, \qquad \tau(t) = \exp\left\{-\left(\frac{t-90}{30}\right)^2\right\}.$$

These forcing functions are chosen to be physically reasonable but of short duration. We examine both forcing functions to investigate possible dependence of the response of the atmosphere on the shape of the impulse.

We treat V as a tunable parameter that determines the total energy deposited into the atmosphere by the forcing function. Our general approach will be to tune V so that some aspect of the simulated phenomena matches observations and compare other aspects of the simulation. For example, we may choose a V that causes the transition region to rise to around 6×10^6 m and study the resulting particle oscillations, atmospheric profiles and shock wave development. Different atmosphere models will require different values of V to raise the transition region to this height.

For simplicity we assume that the solar atmosphere is entirely composed of hydrogen.

4.1. Tests of the numerical method

4.1.1. Accuracy and comparison of the reconstructions

We first check the accuracy of the second- and third-order interpolants described in Section 3.2 on an irregular grid. Table 1 shows the relative L^1 errors for the linear advection problem

$$q_t + q_x = 0, \tag{4.1}$$

with periodic boundary conditions. The errors are shown at $T = 1$ for the periodic initial data $q(x, t = 0) = \sin^4(\pi x)$ on the domain $[-1, 1]$ with nodes at $x_j = x_{j-1} + \Delta(1 + \sin(2\pi j/N)/1.1)$, where N is the number of grid nodes. Here $\Delta = 1/(N-1)$.

Table 1
Relative L^1 errors and convergence rates for the reconstructions on irregular grids used in the scheme (3.3) applied to the advection equation (4.1)

N	Second-order reconstruction		Third-order reconstruction	
	L^1 error	Rate	L^1 error	Rate
50	3.32×10^{-1}	–	8.69×10^{-2}	–
100	1.00×10^{-1}	1.73	1.37×10^{-2}	2.66
200	2.95×10^{-2}	1.76	2.20×10^{-3}	2.64
400	8.93×10^{-3}	1.72	3.79×10^{-4}	2.54

We now compare the quality of the second- and third-order reconstructions for our simulations of the solar atmosphere. Fig. 3 shows the result at $t = 360$ s, initialized using the quiet sun model and perturbed with the square impulse with amplitude $V = 20$ m/s. The second- and third-order methods, were tested with a resolution of 1000 grid nodes in the lower atmosphere region. We see that there is only a small difference between the second- and third-order methods at this resolution. Also notable in this figure is the strength of the shock in velocity value. It is these large velocity shocks that cause the uplift and particle oscillations.

Based on these results we will perform the rest of the simulations in this section with 1000 grid nodes in the lower atmosphere region using the second-order method. We make this choice primarily because of the superior non-oscillatory properties of the second-order method, and also because of its increased speed. Using 1000 grid nodes for our lower atmosphere region of interest (see Section 3.6) give us a resolution of 10 km per grid cell. This is larger than the smallest spacing of 2 km in the VAL model at the transition region, but we find that further refinement of the grid does not significantly alter our results.

4.1.2. Test of numerical hydrostatic balance

As a test of the numerical hydrostatic balance described in Section 3.4, we run the quiet sun model in our simulation conditions with no initial velocity perturbation, i.e. with initial velocity set to zero everywhere. After $t = 4000$ s, the duration of our simulation runs, the velocity is bounded by $|u| < 2 \times 10^{-10}$ m/s, which is consistent with roundoff error in terms of the internal units used in our computations. Similar results are found with the other atmosphere models. Thus numerical hydrostatic balance is preserved.

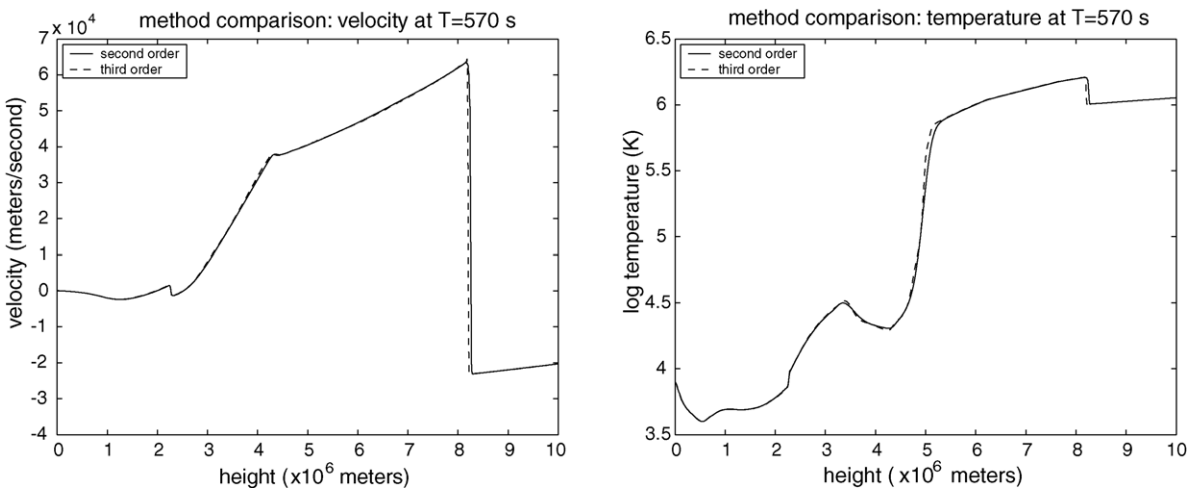

Fig. 3. Comparison of second- and third-order methods. Left: velocity; right: temperature.

4.2. Spicule formation

Spicules are narrow near-linear features that are observed on the solar limb [3,13] (see Fig. 2). They are observed to rise with upward velocities of about 25 km/s, have temperatures in the range of 5000–10,000 K and densities of about 3×10^{-10} kg/m^3. Their maximum height is between 6.5×10^6 and 9.5×10^6 m. Because of these relatively low temperatures and high densities, spicules can be thought of as an intrusion of chromospheric material into the corona. Their linear shape can be explained as this material being channeled inside a magnetic flux tube.

We are primarily interested in the behavior of the transition region in response to impulses at the base of the atmosphere, as well as the physical conditions below the transition region at its time of maximum height. We define the position of the transition region to be where the temperature rises through 200,000 K. We compare simulations using the three atmosphere models with both square and Gaussian impulses. We do this despite the fact that spicules are not observed above sunspots in order to study the dependence of spicule formation on the atmosphere model.

The dominant feature of our simulations is strong initial and rebound shock waves that repeatedly appear for as long as 30 min after the single initial impulse. An example of the effect of these shocks on the quiet sun model is shown in Fig. 4.

We first study the comparative response of the three model atmospheres to the same impulse amplitude. We set the impulse amplitude to $V = 16$ m/s, which lifts the transition region in the quiet sun atmosphere model to about 6×10^6 m. Impulses with these amplitudes cause velocities in the range of 1 km/s in the lower chromosphere, in accordance with observation. The resulting shock trajectories for all thee models and both square and Gaussian impulses are shown in Fig. 5. We see a characteristic increase in speed as the shock crosses the transition region

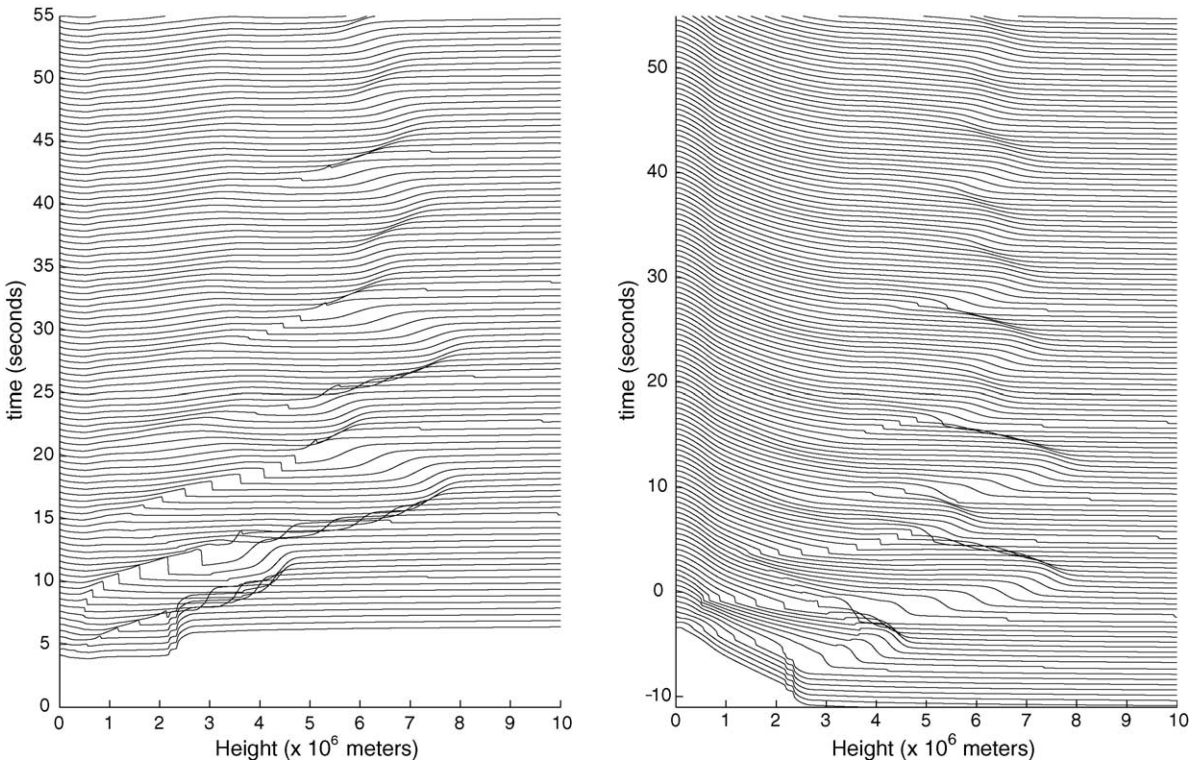

Fig. 4. History of the temperature (left) and density (right) profile for the quiet sun model in response to a square impulse with an amplitude of 20 m/s.

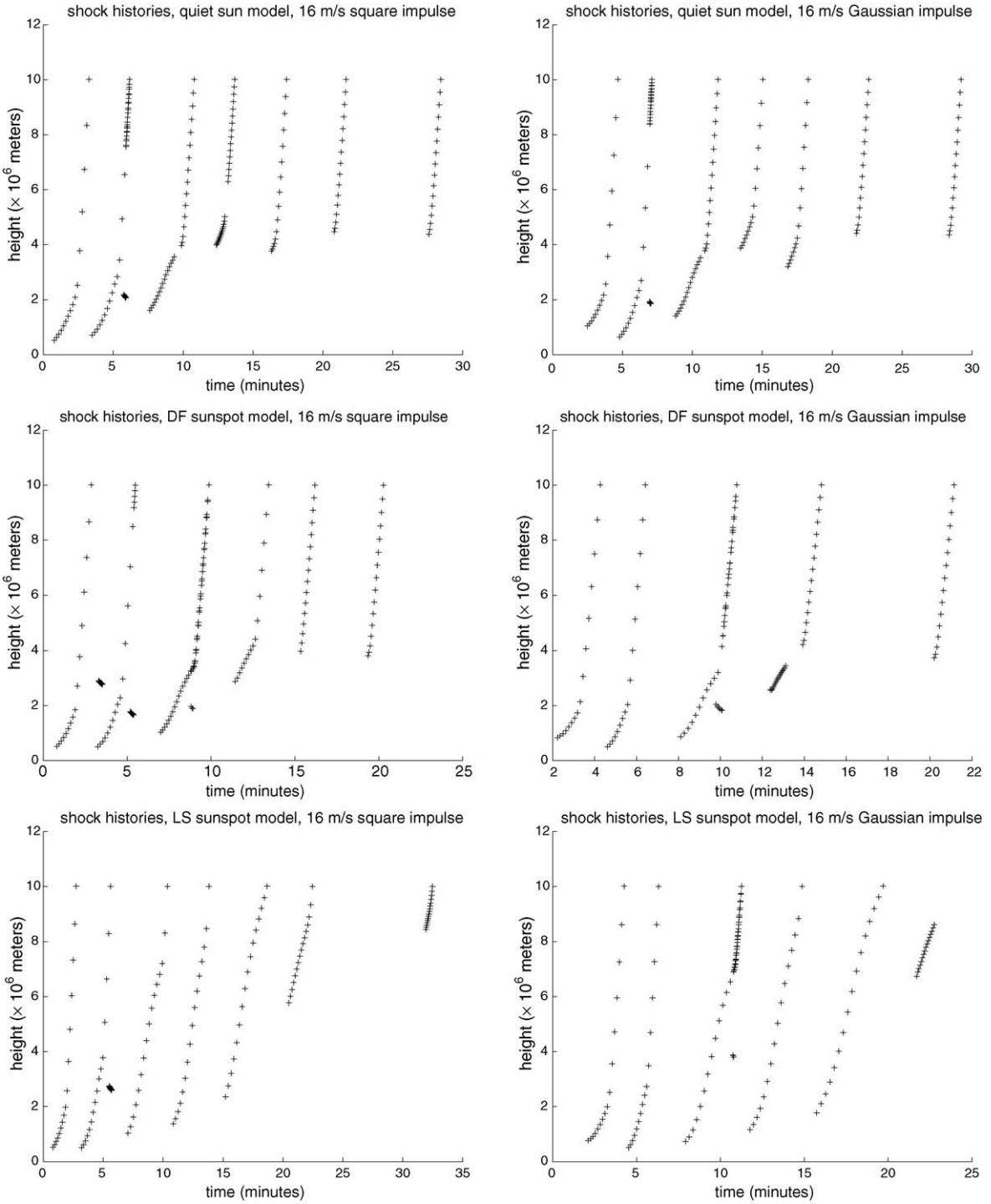

Fig. 5. The trajectories of the velocity shocks for an impulse amplitude of 16 m/s. Left: square impulse; right: Gaussian impulse; top: quiet sun model; middle: Ding–Fang sunspot model; bottom: Lites–Skumanich sunspot model. Note the downward propagating shocks.

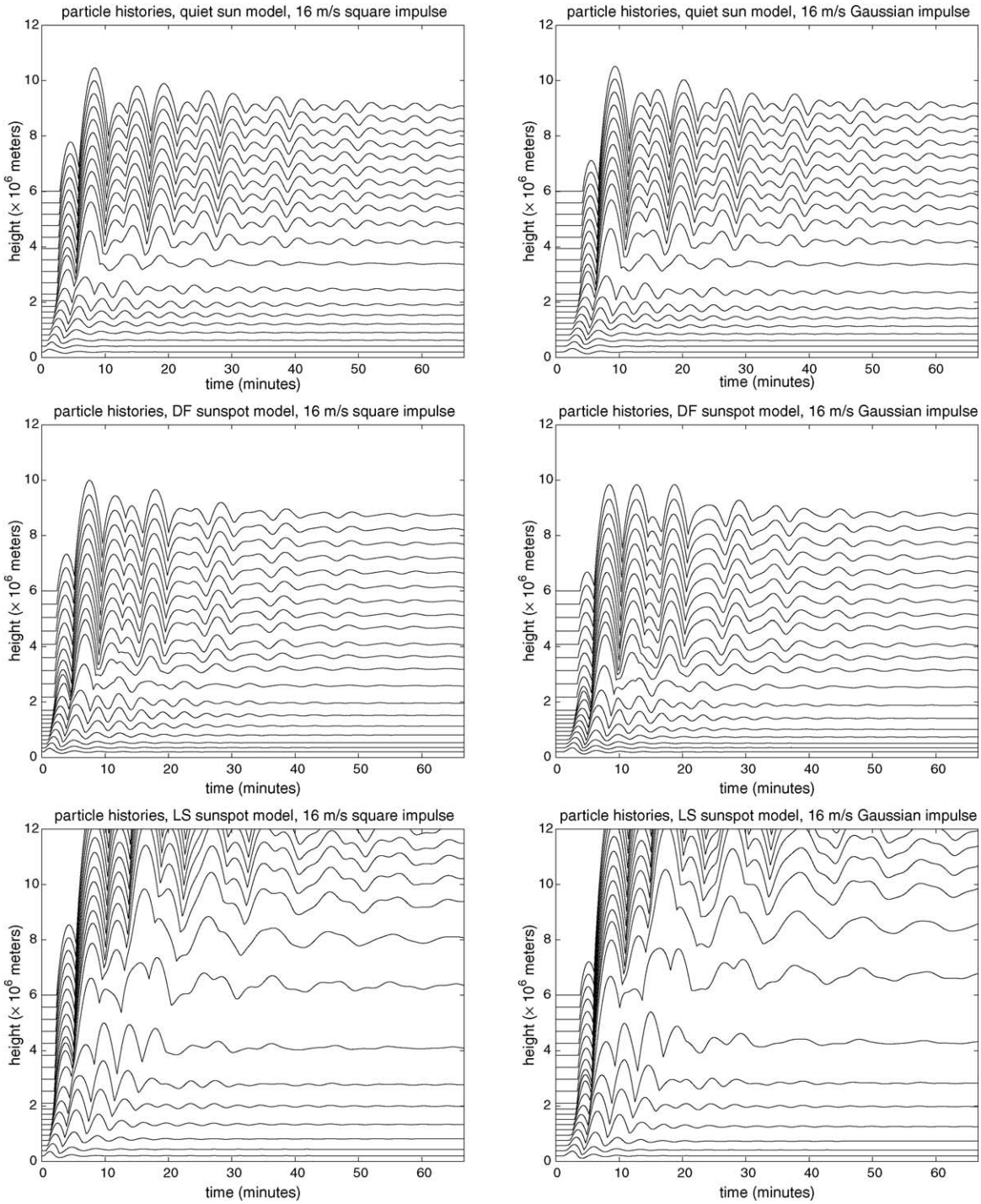

Fig. 6. Particle trajectories for an impulse amplitude of 16 m/s. Left: square impulse; right: Gaussian impulse; top: quiet sun model; middle: Ding–Fang sunspot model; bottom: Lites–Skumanich sunspot model.

from the chromosphere to the corona. As time passes, this increase in speed occurs at higher altitudes as the transition region rises. We also see short-lived downward propagating shocks below the transition region. As seen in Fig. 3, velocity behind the shock reaches as much as 60 km/s as the shock passes the transition region. This causes a dramatic uplift, i.e. lifting material and the transition region well into the initial corona. We track the motion of atmospheric material by seeding test particles at specific heights, then tracking their motions throughout the simulation. The position $x(t)$ of these particles is updated at each time step by solving the ODE $x'(t) = u(x, t)$ via the standard fourth-order Runge–Kutta method, where $u(x, t)$ is the velocity component of the approximated solution. The resulting particle histories is shown in Fig. 6.

We see immediately from Fig. 6 that the Lites–Skumanich sunspot model is much more responsive to the initial impulse, with much higher uplift than the other two models. This is striking since, as seen in Fig. 1, the Lites–Skumanich model has a transition region height intermediate between the other two models. We will discuss a possible mechanism for this increased lift below in Section 4.2.1. This behavior is also evident in Fig. 7, which shows the maximum height of the transition region for varying impulse amplitudes. The three models exhibit a near-linear dependence on impulse amplitude, with the Lites–Skumanich sunspot model showing a greater slope. We see that, particularly for the quiet sun and Ding–Fang atmosphere models, the transition region is lifted to spicule heights, between 5×10^6 and 10×10^6 m, for a wide range of impulse amplitudes. In contrast, the Lites–Skumanich sunspot model is lifting to spicule heights for a narrower range of smaller impulse amplitudes.

Fig. 8 shows estimates of the speed of the transition region in its initial rise for varying impulse amplitudes. This estimate is defined as the height of the first local maximum divided by the time taken to reach that height from first motion. In all cases the speed of the rise increases approximately linearly with amplitude. For the square impulse we see that for the range of impulse amplitudes that produces spicule height transition regions we have speeds just below 20 km/s, just below the average observed value of 25 km/s. For the Gaussian impulse we have somewhat lower speeds.

Fig. 9 shows physical conditions, specifically temperature and density, below the transition region at time of maximum rise for each atmosphere model, with square and Gaussian impulses. In this case we choose impulse amplitudes that lift the transition region to about 6×10^6 m, typical spicule heights, in each model. For the quiet sun, this requires $V = 16$ m/s, the Ding–Fang sunspot model $V = 20$ m/s, and for the Lites–Skumanich model $V = 8$ m/s. The properties observed from this figure are summarized in Table 2, where we see that our simulations match the observations reasonably well.

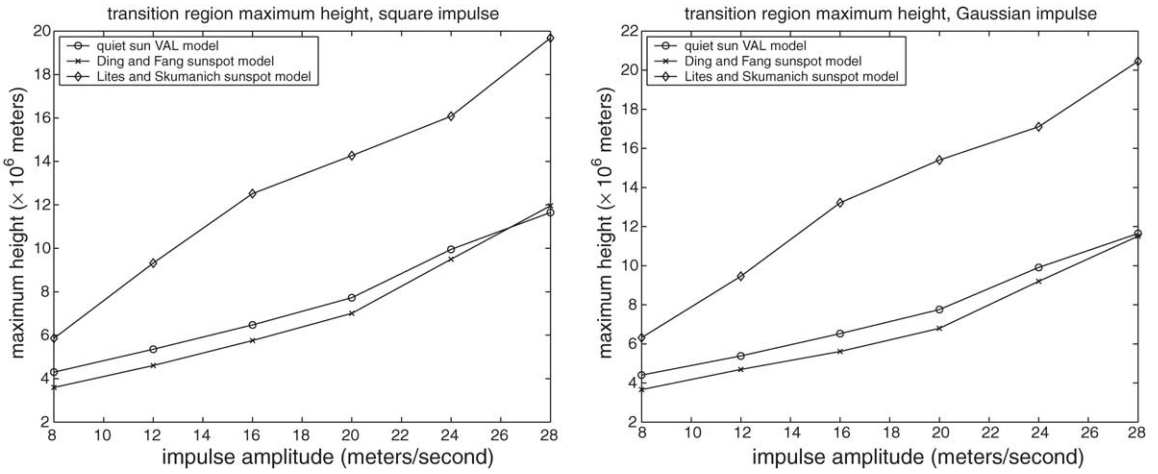

Fig. 7. Maximum height of the transition region for various impulse amplitudes. Left: square impulse; right: Gaussian impulse.

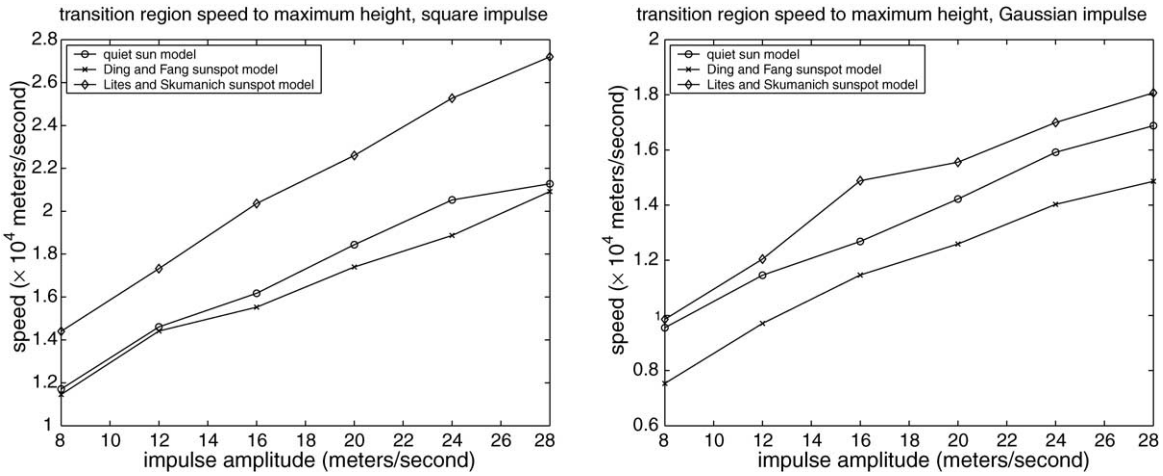

Fig. 8. Average speed of rise of the transition region from initial position to first peak height vs. impulse amplitude. Left: square impulse; right: Gaussian impulse.

4.2.1. Causes of the lifting of the transition region

Our results show that the amount by which the transition region is lifted has a complicated relationship with the atmosphere model. In this section we attempt to understand this relationship. We first study the forces acting at the transition region in an effort to understand the particle histories in Fig. 6. We then study two aspects of the dependence of the atmospheric lifting on the temperature profile: dependence on the temperature in the lower chromosphere, and dependence on the initial height of the transition region. These considerations are motivated by an attempt to understand the increased lift of the corona in the Lites–Skumanich sunspot model, where we have a slightly lower transition region and a cooler chromosphere than the other two models (see Fig. 1).

4.2.1.1. Forces acting on the transition region. We study the forces acting at the transition region by estimating the pressure gradient force F_p and comparing the resultant acceleration $a_p = F_p/\rho$ with the gravitational acceleration g. Fig. 10 plots the ratio a_p/g overlaid on the trajectory of the transition region. We see that for the first several minutes there are large transient accelerations, two orders of magnitude larger than g, caused by the passage of shocks through the transition region. These transient accelerations cause the upward motion of the transition region. Between these pulses a_p drops to an order of magnitude less than g, so the motion of the transition region is nearly, but not completely, ballistic. After 30 min, the acceleration attains a more wave-like character, with neither large nor small accelerations relative to g, so the motion is no longer ballistic. Therefore there seem to be two phases of motion: an early phase dominated by the passage of nonlinear shocks with nearly ballistic motion between the shocks, and a later stage which has more linear wave-like behavior. This is to be expected since the rebounding of the atmosphere damps over time.

Table 2
Temperature and density below the transition region at time of maximum rise based on Fig. 9 compared with observed spicule properties

	Obseved	Square impulse			Gaussian impulse		
		VAL	DF	LS	VAL	DF	LS
Temperature (K)	0.5×10^4 to 10^4	10^4	10^4	$(2–3) \times 10^4$	10^4	10^4	$(2–3) \times 10^4$
Density (kg/m^3)	3×10^{-10}	2×10^{-10}	10^{-9}	10^{-9}	2×10^{-10}	10^{-9}	10^{-9}

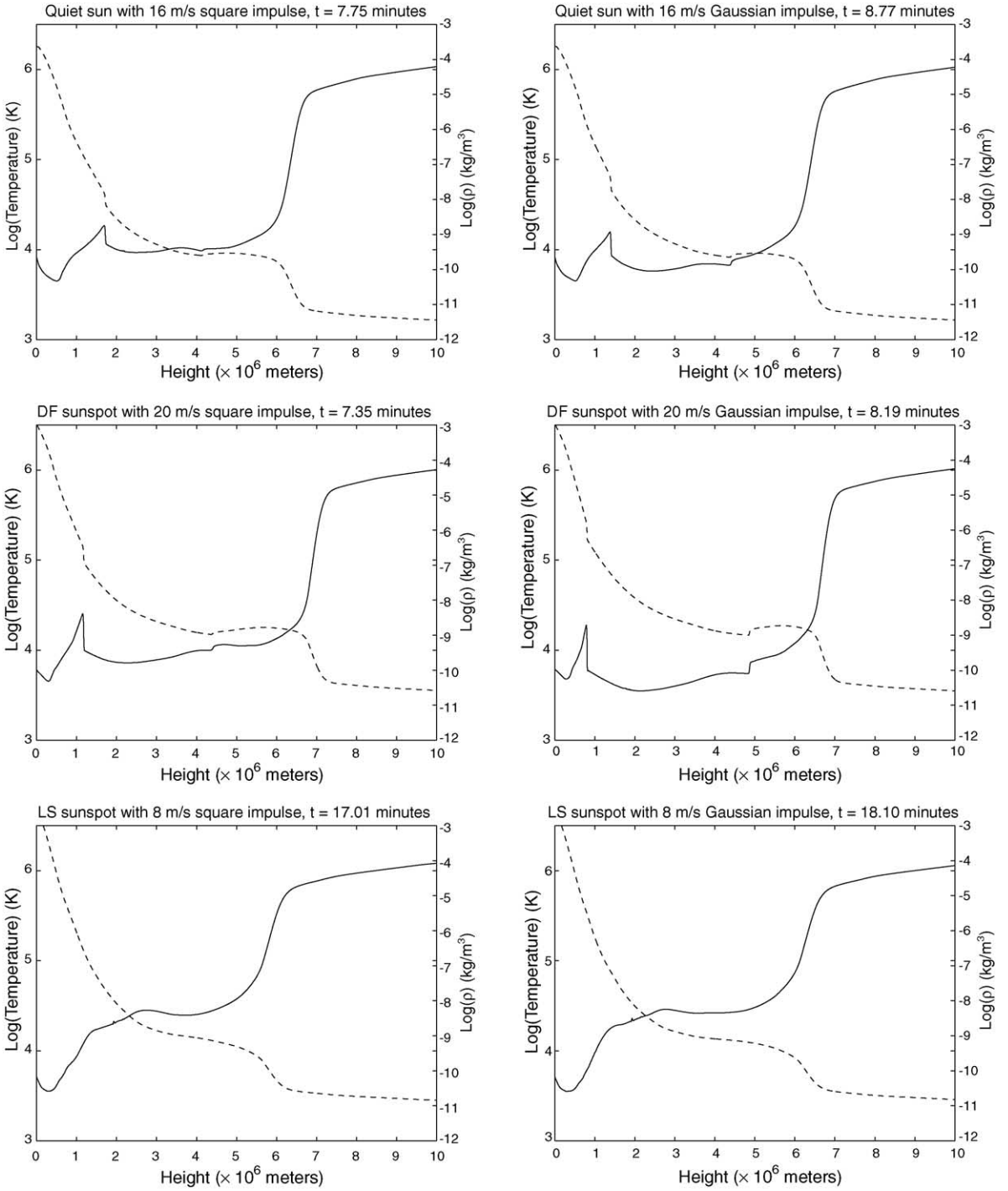

Fig. 9. The temperature (solid line) and density (dashed line) profiles at the time of maximum transition region height. Left: square impulse; right: Gaussian impulse; top: quiet sun model; middle: Ding–Fang sunspot model; bottom: Lites–Skumanich sunspot model.

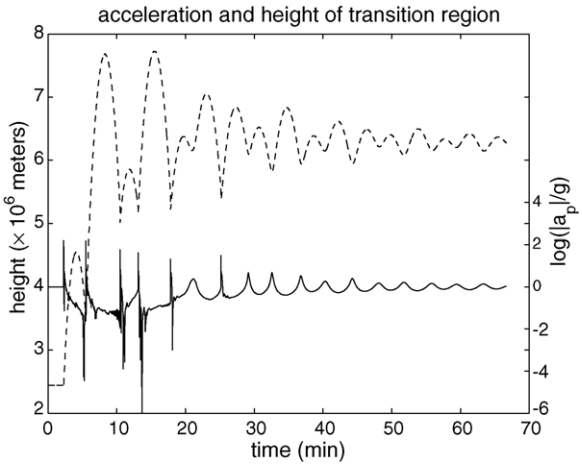

Fig. 10. The trajectory of the transition region (dashed line) and the ratio of the acceleration a_p at the transition region due to the pressure gradient force to the gravitational acceleration g (solid line).

4.2.1.2. Effect of a reduced temperature in the chromosphere. We begin by considering a simple model of an isothermal chromosphere, with temperature T_0, modeled as an ideal gas so $p(x) = R'T_0\rho(x)$. Then the condition for hydrostatic equilibrium (3.9) becomes

$$\frac{\mathrm{d}\rho(x)}{\mathrm{d}x} = -\frac{g(x)\rho(x)}{R'T_0}. \tag{4.2}$$

Therefore an isothermal atmosphere in hydrostatic equilibrium has a density that decreases with height at a rate that is inversely proportional to the temperature. Consider now a given velocity impulse at the base of this atmosphere. As that impulse propagates upwards, conservation of momentum implies that as density decreases the velocity will increase, with the rate of increase being greater for lower temperatures. The higher velocities cause a higher uplift. Simple numerical experiments, replacing the quiet sun VAL temperature profile with a constant temperature chromosphere, confirms that lower-temperature chromospheres exhibit higher lifting of the transition region for a given velocity impulse.

We conjecture that, in a non-isothermal atmosphere, the same mechanism will, at least to a first approximation, cause higher lifting for lower average chromosphere temperature and fixed transition region height. As a simple test of this conjecture, we modified the quiet sun VAL model, suppressing the temperature in the lower chromosphere similarly to the Lites–Skumanich chromosphere, approximately preserving shape (Fig. 11, left). The resulting particle histories for the modified VAL model exhibit significantly increased uplift (Fig. 11, right) as compared with the unmodified VAL model for the same conditions shown in Fig. 6. As expected, the period of coronal oscillation is also larger for the modified VAL model, due to the larger amplitude of the initial lift.

4.2.1.3. Effect of moving the transition region. In an attempt to understand the role that the location of the transition region plays, we present simulations in which the quiet sun model is scaled so that the transition region has various heights. We use a square 20 m/s impulse for this study.

In Fig. 12 we show the dependence of the maximum transition region height on the initial transition region height. We see that there is a nonlinear dependence, where initially higher transition regions get lifted much higher. One possible explanation is that as the pressure shocks pass the transition region, the pressure gradient force will cause an upward acceleration of the transition region like those shown in Fig. 10. Density decreases with height (due to the requirement of approximate hydrostatic equilibrium), so the pressure gradient force will cause greater upward

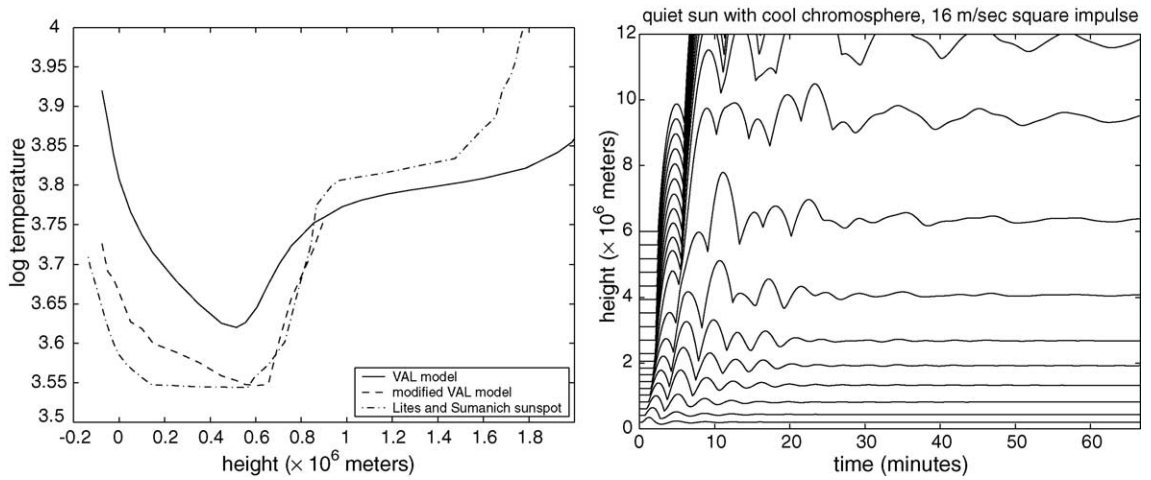

Fig. 11. Left: the chromospheric temperature profiles of the quiet sun VAL, modified VAL and Lites–Skumanich atmosphere models. The modified VAL model has a reduced temperature in the lower chromosphere. Right: the particle histories for the modified quiet sun VAL model in response to a square, 16 m/s impulse, exhibiting increased uplift (compare Fig. 6).

acceleration of higher transition regions. The resulting quasi-ballistic motion of the transition region will lift it to greater heights.

4.2.1.4. Combined effects. The Lites–Skumanich and Ding–Fang sunspot models have both cooler chromospheres and lower transition regions, so we must consider the above effects in combination. This is difficult to do, even qualitatively, because a cooler chromosphere and lower transition region have opposite effects with respect to the amount of lifting. Further, the detailed shape of the temperature profile will have an effect on the amount of lift. We note that the Ding–Fang sunspot model has a somewhat higher temperature in the lower chromosphere, and lower transition region than the Lites–Skumanich model (see Fig. 1). We therefore expect the amount of lift in the

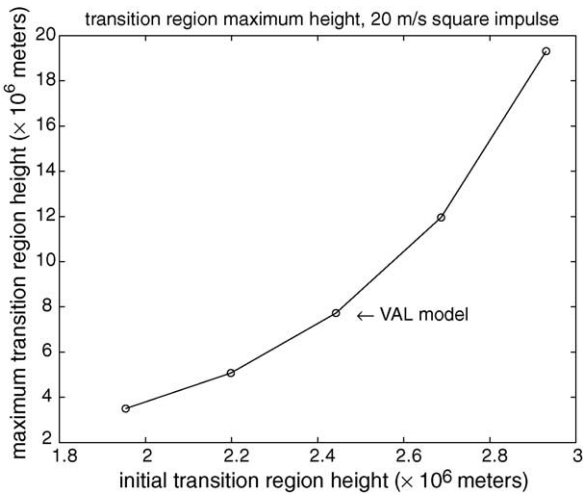

Fig. 12. Maximum height of the transition region in response to a square impulse of 1000 m/s as a function of the initial transition region height in a scaling of the quiet sun model.

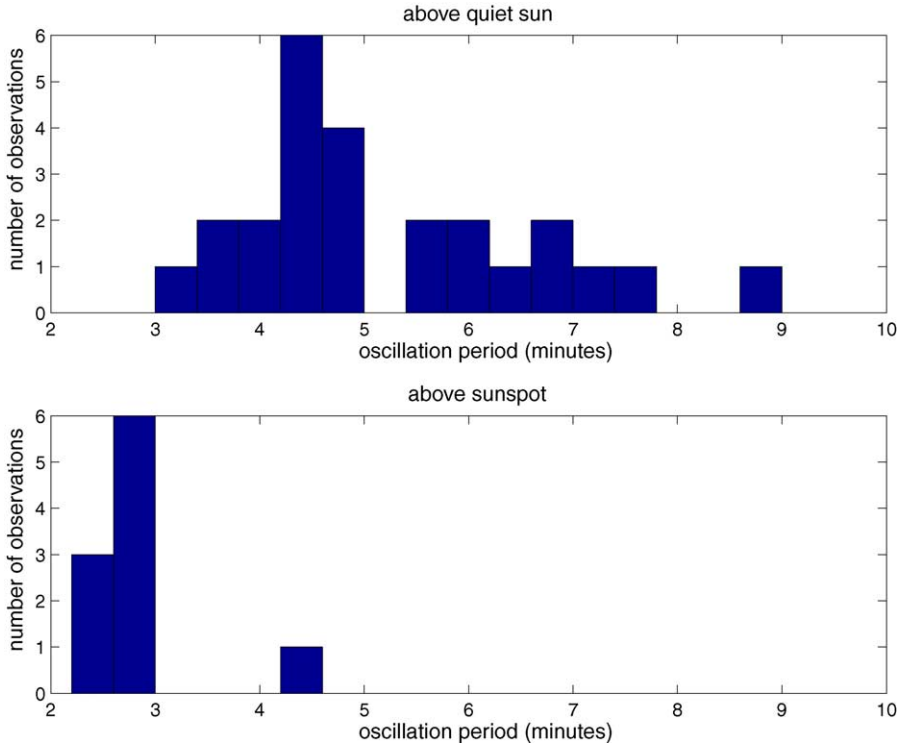

Fig. 13. Histograms of observed periods of coronal oscillations. Top: above the quiet sun; bottom: above sunspots.

Ding–Fang model to be less than in the Lites–Skumanich model. To understand the fact that the Lites–Skumanich model has higher uplift than the quiet sun model, we conjecture that the increased lift due to the lower average chromospheric temperature in the Lites–Skumanich model dominates the decreased lift due to the lower transition region.

In all cases, the higher velocities behind a shock when it reaches the transition region will lead to higher uplift. These higher velocities may be due to the shape of the initial temperature profile, as described above, or due to larger initial velocity impulses, which would explain the results shown in Figs. 7 and 8.

4.3. Coronal oscillations

Recent observations in [2] have detected a notable difference in the period of oscillation of coronal particles above sunspots compared to periods above the quiet sun. Above sunspots, the observed oscillations have periods clustered around 3 min, while above the quiet sun the periods are clustered near 5 min (see Fig. 13).

In our simulations, we find a similar relationship between periods of oscillation of particles in the corona (above the transition region). As seen in Fig. 6, coronal material exhibits an oscillatory behavior after being lifted by the shocks. Due to the multiple shocks this behavior is complex, but there are dominant modes of oscillation. In Fig. 14 we see the power spectra of the particles whose histories are shown in Fig. 6. Here we again choose impulse amplitudes that lift the transition region to typical spicule heights of about 6×10^6 m in each model. We see that for the chosen impulse amplitudes the quiet sun model has a dominant mode of oscillation with a period of 5.6 min, and a weaker mode at about 3.5 min. In contrast, the Ding–Fang and Lites–Skumanich sunspot atmosphere models only has the mode with a period of about 3.5 min. This is consistent with the observational data in Fig. 13.

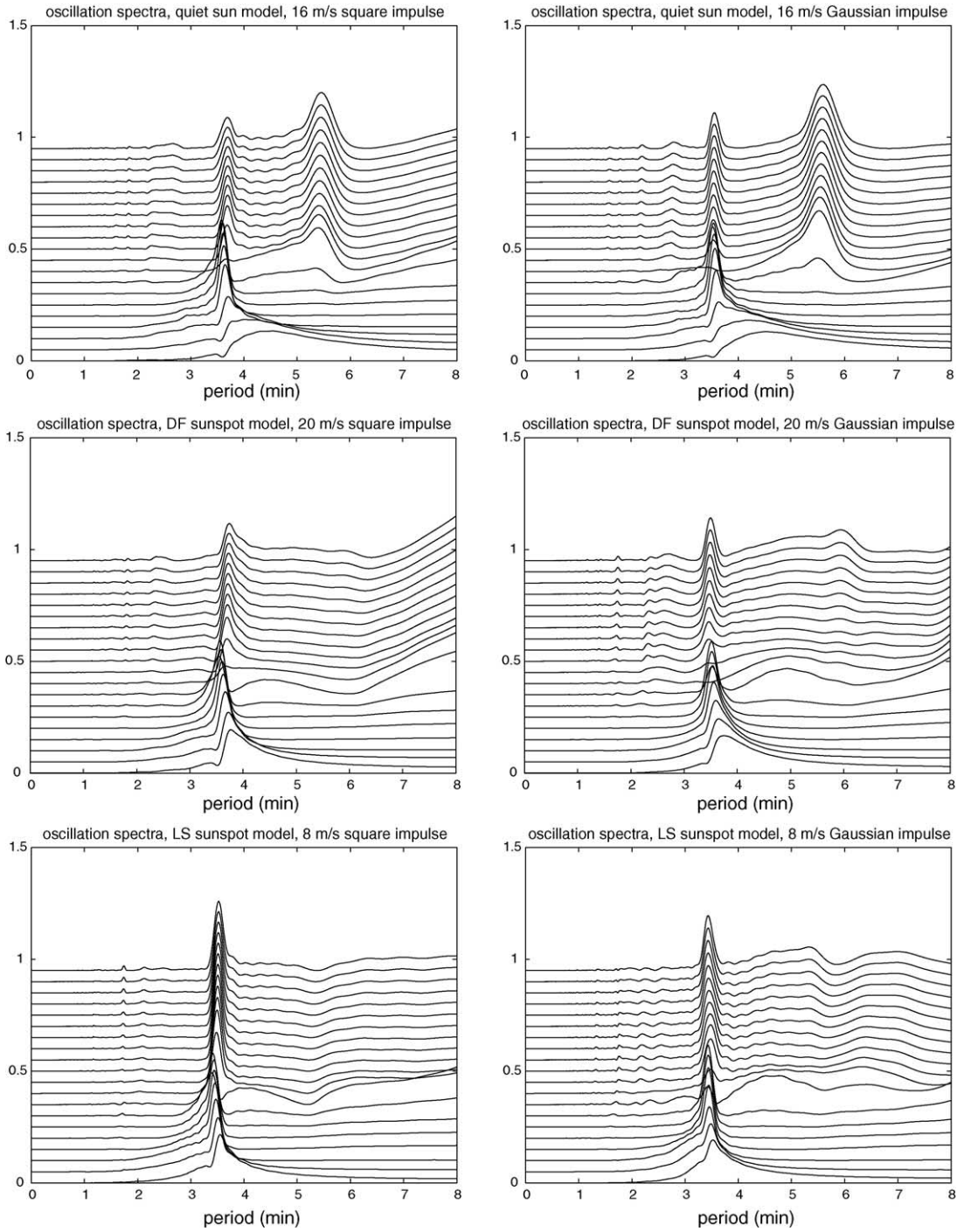

Fig. 14. Particle spectra of particle oscillations for an impulse amplitude which lift the transition region to about 6×10^6 m. The spectra are stacked in order of the height of the particles. Left: square impulse; right: Gaussian impulse; top: quiet sun model; middle: Ding–Fang sunspot model; bottom: Lites–Skumanich sunspot model.

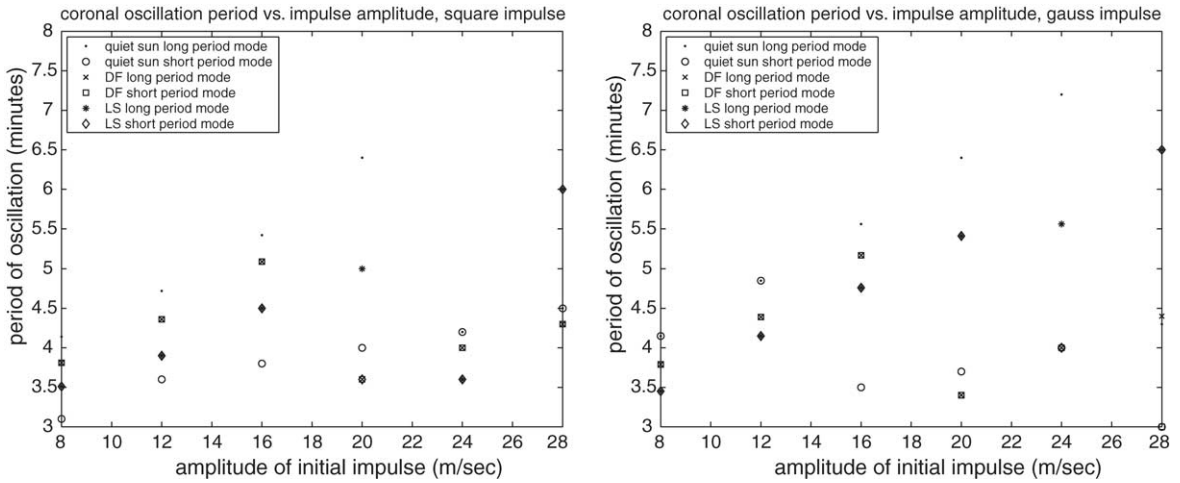

Fig. 15. The simulated periods of oscillations for the three atmosphere models and various surface velocity perturbation amplitudes. Left: square impulse; right: Gaussian impulse.

In general, the period of oscillations of coronal particles depends on the impulse amplitude, though the details of this dependence differs between the atmosphere models. This dependence is summarized in Fig. 15. We see that, generally speaking, the period of oscillation increases with impulse amplitude until a cutoff period of 5–6 min is reached, after which shorter period modes appear and the longer period modes are damped out. For some of our simulations two modes appear, which we interpret to be the suppression of the longer period mode as it approaches the cutoff frequency, so the energy of oscillation goes into shorter-period modes.

5. Conclusions

In this paper we use a high-order shock-capturing scheme to study the response of various one-dimensional model solar atmospheres to a single impulse at the solar surface. While there are many methods for approximating the solutions of the evolution equations used in our study, high-order, non-oscillatory central schemes have the advantage of avoiding Riemann solvers and characteristic variables, which make them well suited for balance laws. Our treatment includes an extension of existing central methods to irregular grids and a new choice of variables which facilitates the numerical maintenance of initial hydrostatic balance. These new features allow us to treat a highly stratified atmosphere, where the density and temperature change over several orders of magnitude with high gradients. Combined with high-resolution and numerical accuracy, our scheme has the ability to detect the effects of subtle differences in initial conditions. Also, the study of particle oscillations is made possible by our ability to resolve and track long trains of shock waves.

The results of our simulations verify the shock-rebound effect suggested in previous work [1,5,6,14] as a possible mechanism of spicule formation. In this model an initial perturbation at the base of the atmosphere causes an acoustic wave that forms into a compression shock as it rises. This is most apparent in the velocity field, where the shock increases dramatically in amplitude as the density decreases with increasing height. By the time the shock reaches the transition region, the velocity amplitude is over 10^4 m/s, which causes a strong lift of the transition region and the underlying material. The shock also heats the gas as it passes. After the initial shock, material falls due to gravity, causing an eventually decreasing train of new compression shocks to form. Due to the energy deposition of the shocks and our neglect of energy loss terms, the atmosphere generally rises, so the particles eventually stabilize at a new height above their original height. As in previous studies, at time of maximum uplift

we find properties of the atmosphere below the transition region that roughly correspond to those observed for spicules.

Particles in the chromosphere and corona are also lifted by passing shocks, which then fall under gravity until the next shock arrives, or in later stages being lifted by pressure waves. The result is particle oscillations in both the chromosphere and corona. From Figs. 5 and 6 we see that during the lifting phase with strong shocks, new shocks arrive before the particles have completed a complete period of oscillation due to buoyancy. This suggests that the timing of the shock waves is the dominant factor in the period of coronal particle oscillations due to rebound shocks.

In spite of the simplicity of our model, we find a remarkable correspondence between our results and observation. We use single impulses whose amplitudes are selected to lift the transition region to spicule heights, around 6×10^6 m. We then observe the response of the solar atmosphere through physical characteristics such as temperature and density below the transition region, the speed at which the transition region rises and the period of oscillation of coronal particles. In all cases our results are consistent with observation. When we vary the impulse amplitude we find that these results do not depend strongly on the specific choice of impulse amplitude. There is also a small but easily observable difference between the results for a square versus a Gaussian impulse.

These results do depend strongly on the atmosphere model. In particular we observe that the particle oscillation spectrum using the quiet sun model differs from the particle oscillation spectrum obtained when a sunspot atmosphere model is used. The differences we observe are consistent with observation of oscillations in the real solar corona. We also note that the amount by which an impulse lifts the atmosphere is strongly dependent on the atmosphere model. Simple experiments show that the temperature of the chromosphere and the location of the transition region are strong determinants of the amount by which the atmosphere will be lifted by a given impulse.

We also examine the balance of forces at the transition region during the rebound-shock train. We find that during the early phases, the motion of the transition region is determined by transient accelerations due to shock passage with intervening periods of near-ballistic motion. At later times, as the rebound phenomena damps out, these forces have a more wave-like behavior.

The next steps in our study include adding energy loss and heating models to our simulations such as in [14]. This will allow us to study the atmospheric response to continuous surface forcing, which in our current model cause the atmosphere to lift without bound due to the continuous energy deposition. Simulations in two-dimensional will follow, where the model will be extended to the magnetohydrodynamic equations.

Acknowledgments

We would like to thank the helpful comments of our anonymous reviewers, which greatly enhanced the quality of this paper. The work of D.L. was supported in part by the National Science Foundation under Career Grant No. DMS-0133511.

References

[1] A.S. Andreev, A.G. Kosovichev, On a mechanism of spicule formation by shock waves in magnetic tubes, Astron. Lett. 403 (1994) 323–326.
[2] I. De Moortel, J. Ireland, A.W. Hood, R.W. Walsh, The detection of 3 & 5 minute period oscillations in coronal loops, Astron. Astrophys. 387 (2002) L13–L16.
[3] B. de Pontieu, Ph.D. Thesis, University of Ghent, Belgium, 1996.
[4] M.D. Ding, C. Fang, A semi-empirical model of sunspot penumbra, Astron. Astrophys. 235 (1989) 204–212.
[5] J.V. Hollweg, On the origin of solar spicules, ApJ 257 (1982) 345–353.
[6] A.G. Kosovichev, Yu.P. Popov, The computation of one-dimensional non-stationary problems of gravitational gas dynamics, USSR Comput. Math. Math. Phys. 19 (1978) 168–175.
[7] K. Kurganov, G. Petrova, A third-order semi-discrete genuinely multidimensional central scheme for hyperbolic conservation laws and related problems, Numer. Math. 88 (2001) 683–729.

[8] K. Kurganov, S. Noelle, G. Petrova, Semi-discrete central-upwind schemes for hyperbolic conservation laws and Hamilton–Jacobi equations, SIAM J. Sci. Comput. 23 (2001) 707–740.
[9] B.W. Lites, A. Skumanich, A model of a sunspot chromosphere based on OSO 8 observations, ApJS 49 (1989) 293–316.
[10] X.-D.L. Liu, S. Osher, Nonoscillatory high order accurate self-similar maximum principle satisfying shock capturing schemes I, SIAM J. Numer. Anal. 33 (2) (1996) 760–779.
[11] K. Shibata, Y. Suematsu, Why are spicules absent over plages and long under coronal holes?, Solar Phys. 78 (1982) 333–345.
[12] C.-W. Shu, S. Osher, Efficient implementation of essentially non-oscillatory shock-capturing schemes, J. Comput. Phys. 77 (1988) 439–471.
[13] A.C. Sterling, Solar spicules: a review of recent models and targets for future observations, Solar Phys. 196 (2000) 79–111.
[14] A.C. Sterling, J.T. Mariska, Numerical simulations of the rebound shock model for solar spicules, ApJ 349 (1990) 647–655.
[15] Y. Suematsu, K. Shibata, T. Nishikawa, R. Kitai, Numerical hydrodynamics of the jet phenomena in the solar atmosphere. I. Spicules, Solar Phys. 75 (1982) 99–118.
[16] P.K. Sweby, High resolution schemes using flux limiters for hyperbolic conservation laws, SIAM J. Numer. Anal. 21 (1984) 995–1011.
[17] J.E. Vernazza, E.H. Avrett, R. Loeser, Structure of the solar chromosphere. III. Models of the EUV brightness components of the quiet-sun, ApJS 45 (1981) 635–725.